PAPER

Edge harmonic oscillations in plasmas with a separatrix and the effect of edge magnetic shear

View the article online for updates and enhancements.

Edge harmonic oscillations in plasmas with a separatrix and the effect of edge magnetic shear

G Bustos Ramirez[1,*] , **J P Graves**[1] **and D Brunetti**[2]

[1] École Polytechnique Fédérale de Lausanne, Swiss Plasma Center, CH-1015 Lausanne, Switzerland
[2] CCFE, Culham Science Centre, Abingdon, Oxon OX14 3DB, United Kingdom

E-mail: guillermo.bustosramirez@epfl.ch

CrossMark

Abstract

This work presents an extension of exfernal mode theory, where the effects of edge magnetic shear and plasma separatrix are investigated and applied to edge harmonic oscillations (EHOs). Linear analytical modelling is performed on a large aspect ratio tokamak with circular cross section, from which a set of three coupled differential equations describing the dispersion relation are derived. To correctly assess the effect of edge shear on exfernal modes, higher order corrections need to be retained in the expansion of the safety factor around the rational surface. The equations are solved numerically for equilibrium pressure and safety factor profiles containing the key features for the excitation of exfernal modes, including a model of a plasma separatrix. The current-driven branch of the instability is significantly reduced by the inclusion of the separatrix, but the mode remains unstable through coupling with the pressure-driven infernal drive. The obtained parameter space for the instability without the effect of the separatrix is compared with the growth rates calculated using the KINX code, and with the nonlinear plasma displacement calculated using the VMEC free-boundary code. From the comparison it was found that the edge shear can be of order unity and still excite exfernal modes, implying that EHOs can be excited even with weak flattening of the local safety factor at the edge, which is in line with some current experimental observations, but contrary to previous simpler analytic theory.

Keywords: edge harmonic oscillations, separatrix, infernal, magnetohydrodynamics, plasma stability

(Some figures may appear in colour only in the online journal)

1. Introduction

One promising ELM-free mode of plasma operation is the so-called Quiescent H-mode (QH-mode), where ELMs are suppressed and instead continuous low wavelength modes called edge harmonic oscillation (EHOs) saturate nonlinearly while sustaining high pedestal pressure [1]. QH-mode operation, and therefore EHOs, are observed in low collisionality regimes, where the large pressure gradient in the pedestal gives rise to increased bootstrap current at the edge, resulting in local flattening of the safety factor in the pedestal region. The increased bootstrap current pushes the equilibrium towards the peeling instability boundary, which would trigger ELMs in a standard H-mode discharge. Such high-n modes are believed to be stabilised linearly by sheared poloidal and diamagnetic $\mathbf{E} \times \mathbf{B}$ flows [2–4], and/or damped in the nonlinear phase [5, 6]. Nevertheless, under such equilibrium conditions low-n external infernal (*exfernal*) modes can grow and saturate. These modes arise from the coupling of external kink and infernal drives,

---

* Author to whom any correspondence should be addressed.

where the latter comes from the combination of low magnetic shear and high pressure gradient over the pedestal region. Linear analytic [2, 7, 8] and numerical [9–11] modelling suggests that EHOs might correspond to the nonlinear saturated state of exfernal modes when a plateau in the safety factor is observed. However, other numerical studies and experimental observations [12, 13] have found MHD structures similar to EHOs in cases where the magnetic shear over the pedestal region is of order unity. This means that analytical exfernal mode theory requires the inclusion of finite edge magnetic shear in order to offer a robust explanation for the excitation of EHOs.

The present paper investigates the effect of finite magnetic shear in the pedestal on the excitation mechanism of low-n exfernal modes. This is done using a semi-analytical approach which extends previous work on exfernal modes [7] in a large aspect ratio tokamak, where now the assumption of having vanishing magnetic shear near the edge is relaxed. This is achieved by expressing the safety factor in the pedestal region as $q(r) = q_s(1 + \Delta q(r)/q_s)$, where $q_s = m/n$ with m and n integers and $\Delta q(r)/q_s \ll 1$. An expansion in $\Delta q(r)/q_s$ is performed including terms of order $\mathcal{O}(\Delta q^1/q_s)$ which account for finite magnetic shear contributions. Note that in previous work such terms are not present [2, 7, 8, 14]. Numerical solution of the equations allows us to solve the exfernal problem for more realistic profiles, while using a simplified large aspect ratio model allows us to keep track of the relevant physics in the equations.

Access to the QH-mode regime is often considered to be related to the presence of toroidal rotation and in particular $\mathbf{E} \times \mathbf{B}$ plasma flow. Experimental evidence [15] shows that $\mathbf{E} \times \mathbf{B}$ flow shear rather than net toroidal flow is what determines the accessibility to QH-mode, which is somewhat recovered by analytical [2] and numerical [3, 16–18] modelling. The impact of toroidal rotation on low-n modes is mainly a Doppler shift of the eigenfrequency, i.e. the introduction of a mode frequency which is proportional to the plasma bulk rotation Ω according to the rule $f \propto n\Omega$ [2, 7], provided Ω is high enough. In such conditions, locked modes that would otherwise terminate the discharge are avoided [12]. In the nonlinear regime, saturated exfernal modes calculated in VMEC show that the derivative of the perturbed poloidal magnetic field (which is what is measured in experiments) persist for various toroidal harmonics. When the correct Doppler shift is taken into account $(d\delta B^\theta/dt \propto n\Omega\delta B^\theta)$ the associated VMEC spectrogram agrees well with experiments [10]. Hence, in our study we drop toroidal rotation in the equilibrium, bearing in mind that the eigenvalue should be Doppler shifted post-calculation if one wishes to treat the dynamics in the laboratory frame. Continuum damping, the interaction with resistive external structures, and kinetic effects which all may affect the dynamics of a rotating mode are not treated in this work, and so are left for a more refined analysis. On the other hand, diamagnetic corrections and $\mathbf{E} \times \mathbf{B}$ poloidal flow shear influences the mode structure of the instability, damping high-n modes while allowing low-n modes to grow, with a modest effect on their growth rate. Such effects are also neglected in the present work as they have been already treated in [2].

Separatrix effects are also modelled in this work by assuming that each resonant surface lies within the plasma by taking $q \to \infty$ as $r \to a$. Such divergence in the safety factor has a strong stabilising influence on edge current driven modes (e.g. peeling modes) [19–21]. However, for instabilities driven both by pressure and current (e.g. peeling-ballooning and exfernal modes) the modes remain unstable in the presence of a separatrix [22]: the current-driven branch becomes weaker or even disappears, while the pressure-driven branch can persist (which is indeed observed in the present study).

The paper is organised as follows: section 2 describes the equilibrium configuration. Using a large aspect ratio expansion, stability equations for the equilibrium configuration are derived in section 3 by taking projections of the vorticity operator applied to the linearised momentum equation. Three coupled differential equations that describe the linear evolution of a main mode (m, n) and its sidebands $(m \pm 1)$ are obtained. Such equations are solved numerically in section 4 and various cases of interest are analysed. Section 5 is devoted to compare the obtained results with well established codes, first against full 3D nonlinear simulations in JET-like geometry using the VMEC free-boundary code, and later against the KINX linear stability code. In section 6 we introduce and implement a simple model of the plasma separatrix, and the exfernal equations are again solved numerically. Finally, section 7 summarises the work and offers conclusive remarks.

2. Equilibrium model

The plasma equilibrium is expanded analytically with respect to small inverse aspect ratio $(a/R_0 \sim \epsilon \ll 1)$ assuming shifted circular cross sections, where a and R_0 are the minor and major radii respectively. The analysis is performed on a right-handed coordinate system (r, θ, ϕ), where r is a flux coordinate with units of length, $\theta(\omega) = \frac{F(r)}{q(r)} \int^\omega \frac{\mathcal{J}_\omega}{R^2} d\omega$ is the straight field line poloidal angle and ϕ the toroidal angle. Here, ω is the geometric angle and $\mathcal{J}_\omega$ is the corresponding Jacobian. Standard tokamak ordering is assumed: $B_P \sim \epsilon B_T$ and $\beta = 2\mu_0 P/B^2 \sim \epsilon^2$, with $\mathbf{B_P} = \nabla\phi \times \nabla\psi$ the poloidal field, $\mathbf{B_T} = F(\psi)\nabla\phi$ the toroidal field, P the plasma pressure, $F(\psi) = RB_\phi$ and $2\pi\psi$ the poloidal magnetic flux.

Equilibrium profiles are chosen so that they reproduce the key aspects of QH-mode operation [23] qualitatively. The pressure profile has an edge pedestal close to the vacuum region, where the pressure gradient associated with the pedestal drives a strong bootstrap current in the low collisionality regime. To separate the driving mechanism of pressure gradient and current density we model the safety factor and magnetic shear to monotonically increase from the core, then the magnetic shear gets weaker in the pedestal region as a consequence of the bootstrap current (figure 1). Variations in the safety factor (or equivalently the edge current density) at the edge can be seen as variations in the edge collisionality at constant pressure gradient, thus avoiding the difficulty of accurately modelling a bootstrap current that is consistent with the
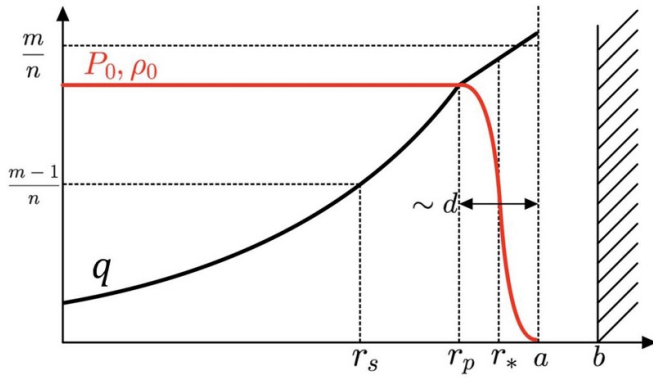
Figure 1. Model of the radial profiles of the safety factor, pressure and density. The weakening of the magnetic shear covers the pedestal region going from r_p to a. Note that the model and analysis do not require the resonance m/n to be at r_*.

pressure profile at constant collisionality. A safety factor profile with the required characteristics is:

$$q(r) = \begin{cases} \dfrac{m-1}{\kappa\left[1 - (r/r_-)^\mu\right] + n} & \text{if } r \leqslant r_p \\ q_*\left[1 - s_*(1 - r/r_*)\right] & \text{if } r \geqslant r_p \end{cases} \quad (1)$$

where r_- is the radius of the lower sideband resonance, μ is a constant that defines how fast q grows in the core region, r_p roughly denotes the radius of the pedestal shoulder, κ is a constant that guarantees continuity of the safety factor at r_p, s_* is the magnetic shear at r_*, $r_* = \frac{1}{2}(r_p + a)$ and $q_* = q(r_*)$.

It is worth to mention at this point that within our ordering the stability properties in the region $[0, r_p]$ are completely determined by current effects rather than pressure or inertial effects. Therefore, we can consider the pressure (and density) to be roughly constant in that region and only model a large gradient in the pedestal region. A suitable analytical expression is given by:

$$\frac{P(r)}{P_0} = \frac{\rho(r)}{\rho_0} = \frac{1}{2}\left[1 - \tanh\left(\frac{4(r - r_*)}{d}\right)\right] \quad (2)$$

with P_0 and ρ_0 the pressure and density at the magnetic axis and d a measure of the pedestal width.

With the pressure profile described above, we may have the ballooning parameter $\alpha = -Rq^2\beta' \sim 1$ in the pedestal region. Nevertheless, the total β can still be of order ε^2 if the pedestal region only covers a narrow region of width $\sim d \ll r$, so that $\beta' \sim \beta/d \sim \epsilon$. In such a scenario, the assumption of concentric flux surfaces still holds [8, 24, 25], and one can consistently use the low-β expansion of the equilibrium equations. We point out that the profiles used in this paper are consistent with these approximations, and that the low-β equations used in this work have yield good results when compared with numerical modelling using QH-mode-like equilibrium profiles [2, 7, 10]. In the limit of high-β or large pressure gradient over a wide section of the tokamak, the model does not hold anymore, and new equilibrium equations have to be derived. This has been done in [8] for exfernal modes, where no major

differences in the solutions where found in cases where the pressure gradient is large only on a narrow region.

3. Stability equations

For the stability analysis we separate the plasma domain into three intervals, delimited by the newly introduced parameters r_1 and r_2, with $0 \leqslant r_1 < r_2 \leqslant a$. We regard the intervals $[0, r_1] \cup [r_2, a]$ as 'high shear' regions, where poloidal coupling is neglected due to the field line bending (FLB) stabilisation dominating in the absence of strong pressure gradients. The interval $[r_1, r_2]$ (roughly, but not exactly equal to $[r_p, a]$ in figure 1) is regarded as a 'low shear' region, where poloidal coupling with neighbouring sidebands is induced through the effect of toroidicity in the geometrical coefficients. We point out that the parameters r_1 and r_2 do not change the equilibrium in any way, and their role is to delimit the regions in which each set of stability equations is to be used. The definition of what can be considered as 'low shear' and 'high shear' is in general vague, though physically meaningful results must be independent of the choice of r_1 and r_2. One way to set r_1 and r_2 is to chose values which maximise the growth rate, which is what is done for example in Reference [26] for infernal modes. In section 4 a *Reference* model is introduced, which contains global coupled equations that are valid in the whole plasma domain, so the most realistic scenario for that model is to chose $r_1 = 0$ and $r_2 = a$.

3.1. High shear region

In the high shear region all modes are independent, and the equation describing the radial plasma displacement for any mode m'/n is given by [27, 28]

$$\frac{1}{r}\frac{d}{dr}\left[r^3\left(\frac{1}{q} - \frac{n}{m'}\right)^2\frac{d}{dr}\xi_r^{(m')}\right] - (m'^2 - 1)$$

$$\times \left(\frac{1}{q} - \frac{n}{m'}\right)^2\xi_r^{(m')} = 0. \quad (3)$$

This is the leading order marginal stability equation in a straight cylinder. The singularity at $q = m'/n$ can be removed by adding finite inertia [29]. The present study neglects inertia effects in the high shear region, and the singularity is avoided by imposing the solution to be finite at its own rational surface. Residual inertia effects in the high-shear region where studied in [8] and concluded to be small for sufficiently low growth rates.

3.2. Low shear region

The driving mechanism for exfernal modes lies within this region, where there is combination of a large pressure gradient over an extended region of low magnetic shear close to the plasma edge, and the safety factor is close to a rational surface at $q \sim q_s = m/n$. A main helical mode (n, m) develops in this region, and couples with the corresponding upper and lower sidebands $(n, m \pm 1)$. The analytical treatment follows the

standard tokamak ordering described in the previous section. Stability equations are derived from the linearised ideal MHD perturbed momentum equation:

$$\vec{L}(\vec{\xi}) = \vec{\mathcal{F}}(\vec{\xi}) + \rho\gamma^2\vec{\xi} = 0, \qquad (4)$$

where $\vec{\xi}(t,r,\theta,\phi) = \vec{\xi}(r,\theta,\phi)e^{i\gamma t}$ is the Lagrangian fluid displacement and ρ is the mass fluid density. The force operator $\vec{\mathcal{F}}(\vec{\xi})$ is given in its covariant form by [27]:

$$\mathcal{F}_i = \delta B^k \partial_k B_i + B^k \partial_k \delta B_i - \Gamma^j_{ik}\left(\delta B^k B_j + B^k \delta B_j\right)$$
$$- \partial_i\left(\delta B^k B_k\right) + \partial_i\left(\xi^k \partial_k P + \frac{\Gamma P}{\mathcal{J}}\partial_k(\mathcal{J}\xi^k)\right), \quad (5)$$

where Γ^j_{ik} are the Christoffel symbols of second kind. The first five terms correspond to the expansion of the terms $\vec{J}\times\delta\vec{B} + \delta\vec{J}\times\vec{B}$, with $\delta\vec{J} = \nabla\times\delta\vec{B}$ the perturbed current and $\delta\vec{B} = \nabla\times(\vec{\xi}\times\vec{B})$ is the perturbed magnetic field (we have normalised $\mu_0 = 1$). The last two terms correspond to the gradient of the perturbed pressure $\nabla\delta P$.

Following Bussac *et al* [30] we separate the fluid displacement as $\vec{\xi}(r,\theta,\phi) = \vec{\xi}_B + \eta\vec{B}$, where $\vec{\xi}_B \cdot \nabla\phi = 0$, $\xi_{(r)} = F\vec{\xi}_B \cdot \nabla r$ and $\xi_{(\theta)} = rF\vec{\xi}_B \cdot \nabla\theta$. Different toroidal harmonics denoted by the toroidal mode number n are decoupled because of toroidal symmetry in the equilibrium, so we can write $\xi(r,\theta,\phi) = \xi(r,\theta)e^{in\phi}$. For simplicity we remove the ϕ dependency in our equations by substituting $\partial_\phi \to in$. We expand the Bussac variables in our large aspect ratio parameter ε as:

$$\xi_{(r)}(r,\theta)$$
$$= \left[\xi^{(m)}_{r0}(r) + \epsilon\left(\xi^{(m+1)}_{r1}(r)e^{-i\theta} + \xi^{(m-1)}_{r1}(r)e^{i\theta}\right)\right]e^{-im\theta} \quad (6)$$

$$\xi_{(\theta)}(r,\theta) = \left[\xi^{(m)}_{\theta 0}(r) + \epsilon\left(\xi^{(m+1)}_{\theta 1}(r)e^{-i\theta} + \xi^{(m-1)}_{\theta 1}(r)e^{i\theta}\right)\right.$$
$$\left. + \epsilon^2\xi^{(m)}_{\theta 2}(r)\right]e^{-im\theta} \quad (7)$$

$$\eta(r,\theta)$$
$$= \eta^{(m)}_0(r) + \epsilon\left(\eta^{(m+1)}(r)e^{-i\theta} + \eta^{(m-1)}(r)e^{i\theta}\right)e^{-im\theta}. \quad (8)$$

The Fourier decomposition considers a dominant harmonic component with poloidal mode number m, and its two sidebands $m \pm 1$ which are formally one order smaller. The higher order $\mathcal{O}(\epsilon^2)$ helical component of the poloidal displacement contains corrections to the lower order $\mathcal{O}(\epsilon^0)$ radial displacement $\xi_{(r)}$. The parallel plasma displacement also considers a main harmonic perturbation and its two smaller sidebands, though the main harmonic vanishes to leading order. It can be shown that this expansion completely describes the perturbation to relevant order [14].

Expressions relating $\xi_{(\theta)}$ and $\xi_{(r)}$ are found by taking the appropriate Fourier components of equation (4) at each order (see for example [31]). The relation between η and $\xi_{(r)}$ is found by projecting the momentum equation in the equilibrium magnetic field $\left(\vec{L}(\vec{\xi})\cdot\vec{B} = 0\right)$, then taking Fourier components

of the resulting equations order by order. The eigenvalue equations for the radial components of the main mode and sidebands in the low shear region are derived by Fourier analysing the toroidal component of the vorticity equation $\mathcal{J}\nabla\times\frac{\vec{L}(\vec{\xi})}{B^\phi}$ [2, 29], with $\mathcal{J}$ the Jacobian in our straight field line coordinate system. This can be written in terms of the covariant components of the momentum equation as:

$$V^\phi(\xi,p) = \frac{1}{2\pi}\int_0^{2\pi}d\theta\left[\partial_r\left(\frac{L_\phi}{B^\phi}\right) + ip\frac{L_r}{B^\phi}\right]e^{ip\theta}. \quad (9)$$

Equations are found order by order for the main mode and sidebands via $V^\phi(r,m)$ and $V^\phi(r,m\pm 1)$ respectively. At order $\mathcal{O}(\epsilon^2)$ we recover the cylindrical equation (3), which describe the main mode of the plasma displacement to relevant order as long as $q - q_s \sim 1$.

The equations at $\mathcal{O}(\epsilon^4)$ include toroidal coupling and pressure, which according to our ordering are only relevant in the vicinity of a rational surface. To formally apply this condition, we write the safety factor as $q(r) = q_s + \Delta q(r)$, where $q_s = m/n$ and $\Delta q/q_s \ll 1$. This allows us to introduce a second ordering in $\Delta q/q_s$. We adapt the ordering notation $\mathcal{O}(\epsilon, \Delta q/q_s)$ to make the distinction between small terms due to the tokamak ordering in large aspect ratio (ϵ) and the small terms due to proximity to the rational surface ($\Delta q/q_s$). The resulting equation for the main mode to order $\mathcal{O}(\epsilon^4, \Delta q/q_s)$ is then: (for details see also in [32])

$$V^\phi_2(\xi,m) + V^\phi_4(\xi_B,m) = \frac{1}{r}\frac{d}{dr}\left[r^3\left(\frac{1}{q} - \frac{1}{q_s}\right)^2\frac{d}{dr}\xi^{(m)}_{r0}\right]$$

$$- (m^2 - 1)\left(\frac{1}{q} - \frac{1}{q_s}\right)^2\xi^{(m)}_{r0} + \frac{\alpha}{q_s^2}\left[\frac{r}{R_0}\left(\frac{1}{q_s^2} - 1\right) - \frac{\alpha}{2}\right]\xi^{(m)}_{r0}$$

$$+ \frac{\alpha}{2q_s^2}\left[\frac{r^{-(1+m)}}{1+m}\frac{d}{dr}(r^{2+m}\xi^{(m+1)}_{r1}) + \frac{r^{-(1-m)}}{1-m}\frac{d}{dr}(r^{2-m}\xi^{(m-1)}_{r1})\right]$$

$$- \frac{\Delta q}{q_s^3}\left\{\Delta'r\frac{d}{dr}\left[\frac{r^{-(1+m)}}{1+m}\frac{d}{dr}(r^{2+m}\xi^{(m+1)}_{r1})\right.\right.$$

$$+ \frac{r^{-(1-m)}}{1-m}\frac{d}{dr}(r^{2-m}\xi^{(m-1)}_{r1})\right] + \left[2(1+m)\frac{r}{R_0} + (1+m)\alpha\right.$$

$$- (4+3m)\Delta'\left.\right]\frac{r^{-(1+m)}}{1+m}\frac{d}{dr}(r^{2+m}\xi^{(m+1)}_{r1}) - \left(\frac{r}{R_0} + \alpha - 4\Delta'\right)$$

$$\times (2+m)\xi^{(m+1)}_{r1} + \left[2(1-m)\frac{r}{R_0} + (1-m)\alpha - (4-3m)\Delta'\right]$$

$$\times \frac{r^{-(1-m)}}{1-m}\frac{d}{dr}(r^{2-m}\xi^{(m-1)}_{r1}) - \left(\frac{r}{R_0} + \alpha - 4\Delta'\right)$$

$$\times (2-m)\xi^{(m-1)}_{r1}\right\} + \left\{\frac{\Delta q}{q_s^3}\left[\frac{4r^2}{R_0^2}\left(2 - \frac{1}{q_s^2}\right) + \frac{3r}{R_0}\alpha\right.\right.$$

$$- \Delta'\left(\frac{6r}{R_0} + 7\alpha - r\alpha'\right) + 12(\Delta')^2\right] - \frac{\Delta q'}{q_s^3}\alpha r\Delta'\right\}\xi^{(m)}_{r0},$$
$$(10)$$

where we make use of the ballooning parameter $\alpha = -\frac{2q_s^2 R_0 P'}{B_0^2}$. The notation $V^\phi_4(\xi_B,m)$ specifies that we have taken into

account only terms coming from the perpendicular plasma displacement. Inertia and compression terms, which are related to the parallel displacement η, are considered in the analysis below. Here we have included the order $\mathcal{O}(\epsilon^2)$ terms (first line), which enter this equation when $q - q_s \ll 1$ (equivalently, when $q - q_s \sim \epsilon$). Therefore, these cylindrical terms are expected to dominate the behaviour of the main mode when $q - q_s \sim 1$. The terms in the second line correspond to the Mercier contribution and the sideband coupling to order $\mathcal{O}(\epsilon^4, \Delta q^0/q_s)$. Order $\mathcal{O}(\epsilon^4, \Delta q/q_s)$ corrections to the main mode component of the plasma displacement appear in the last line of equation (10). The remaining terms couple the main mode with the sidebands at order $\mathcal{O}(\epsilon^4, \Delta q/q_s)$, and can be linked directly to toroidicity (through the r/R_0 parameter), to plasma pressure gradient (through the α parameter) and to magnetic pressure gradient (through the Shafranof shift Δ').

We proceed with the calculation of the sideband equations in the low-shear region (see also in [32])

$$
V_4^\phi(\xi_B, m \pm 1) = \frac{d}{dr}\left[r^{-(1 \pm 2m)} \frac{d}{dr}\left(r^{2 \pm m} \xi_{r1}^{(m \pm 1)} \right)\right]
$$
$$
- 2(1 \pm m)\left\{ \frac{d}{dr}\left[\frac{\Delta q}{q_s} r^{-(1 \pm 2m)} \frac{d}{dr}\left(r^{2 \pm m} \xi_{r1}^{(m \pm 1)}\right)\right]\right.
$$
$$
\left. - (2 \pm m) r^{\mp m} \xi_{r1}^{(m \pm 1)} \frac{\Delta q'}{q_s}\right\} - \frac{1 \pm m}{2}\frac{d}{dr}(r^{\mp m}\alpha \xi_{r0}^{(m)})
$$
$$
+ (1 \pm m)^2 (2 \pm m) r^{-(1 \pm m)}\left(\frac{r}{R_0} + \alpha - 4\Delta'\right)\frac{\Delta q}{q_s}\xi_{r0}^{(m)}
$$
$$
- (1 \pm m)\frac{d}{dr}\left\{ r^{\mp m}\Delta' r \frac{d}{dr}\left(\frac{\Delta q}{q_s}\xi_{r0}^{(m)}\right) - r^{\mp m}\right.
$$
$$
\left. \left[(1 \pm 2m)\frac{r}{R_0} \pm m\alpha - 3(1 \pm m)\Delta'\right]\frac{\Delta q}{q_s}\xi_{r0}^{(m)}\right\}. \tag{11}
$$

We note that the terms proportional to $\xi_{r1}^{(m \pm 1)}$ and derivatives correspond to the expansion in the safety factor of the cylindrical equation (3), keeping corrections up to order $\mathcal{O}(\Delta q^1/q_s)$. As such, they contain the FLB stabilisation contribution of the sidebands. Contrary to the main mode equation, all of the terms are formally order $\mathcal{O}(\epsilon^4)$, meaning that the cylindrical contribution does not dominate the equation even when pushing Δq to larger values. Moreover, because of this the equation gradually loses its validity in the high shear region, so r_1 must remain relatively close to r_p.

To finalise the derivation of the equations we consider the inertial and compression terms at order $\mathcal{O}(\epsilon^4)$. We adopt the following ordering for the growth rate:

$$
\frac{1}{R_0^2}\left(\frac{\gamma}{\omega_A}\right)^2 \sim \epsilon^4, \quad \left(\frac{\omega_s}{\omega_A}\right)^2 \sim \epsilon^2, \quad \frac{\gamma^2}{\omega_s^2} \ll 1, \tag{12}
$$

where $\omega_A^2 = \frac{B_0^2}{\rho R_0^2}$ is the Alfven frequency and $\omega_s = \frac{5P}{3\rho R_0^2}$ is the sound frequency, with B_0, R_0 the magnetic field and cylindrical radii at the magnetic axis. Inertial effects are only important in the near vicinity of the rational surface, where $\Delta q \ll 1$.

Therefore, higher order Δq corrections could in principle be neglected, but for the present work such corrections are included for completeness. Using the expansion of the safety factor and retaining terms up to order $\mathcal{O}(\epsilon^4, \Delta q/q_s)$ gives

$$
V_4^\phi(\eta, m) = \frac{\gamma^2}{m^2}\left\{ (1 + 2q_s^2)\left[\frac{1}{r}\frac{d}{dr}\left(\frac{r^3}{\omega_A^2}\frac{d}{dr}\xi_{r0}^{(m)}\right)\right.\right.
$$
$$
\left. + \xi_{r0}^{(m)}\left(\frac{1 - m^2}{\omega_A^2} + r\frac{d}{dr}\frac{1}{\omega_A^2}\right)\right]
$$
$$
+ 4q_s\left[\frac{1}{r}\frac{d}{dr}\left(\frac{\Delta q r^3}{\omega_A^2}\frac{d}{dr}\xi_{r0}^{(m)}\right) + \xi_{r0}^{(m)}\right.
$$
$$
\left.\left. (1 - m^2)\frac{d}{dr}\left(\frac{r\Delta q}{\omega_A^2}\right)\right]\right\}. \tag{13}
$$

These terms should be added to equation (10), giving an eigenvalue problem for γ^2:

$$
V_2^\phi(\xi, m) + V_4^\phi(\xi_B, m) + V_4^\phi(\eta, m) = 0 \tag{14}
$$
$$
V_4^\phi(\xi_B, m \pm 1) = 0
$$

where we note that since these equations are to be used in a region close to the main mode rational surface, the inertia of the sidebands can be neglected. It is finally emphasised that by neglecting $\mathcal{O}(\epsilon^4, \Delta q/q_s)$ terms (which for the remaining of this work are referred to as 'Δq corrections'), the equations derived in previous papers [7, 14] are recovered.

3.3. Boundary conditions

Equations (14) can be solved given the appropriate boundary conditions. To obtain the eigenvalues (growth rates) and eigenfunctions in the low shear region it is sufficient to know the quantity $\frac{d}{dr}\ln\left(\xi_r^{(m')}\right)$ at the boundaries between the high shear and low shear regions ($r = r_1, r_2$), as well as at the plasma-vacuum interface ($r = a$). The logarithmic derivatives are cast as Robin boundary conditions for equations (14).

3.3.1. Sidebands.
The logarithmic derivative of the upper sideband at the boundary between the high shear and low shear regions can be obtained by solving equation (3) with $m' = m + 1$ from $[0, r_1]$ assuming that the perturbation at the magnetic axis does not diverge. The rational surface of the lower sideband lies in the high shear region, meaning that equation (3) with $m' = m - 1$ is singular at the rational surface. To avoid the singularity, the equation for the lower sideband is solved in the open interval $(r_-, r_1]$, where we recall that r_- is the radius of the rational surface. For the profile defined in equation (1) analytical solutions exist and are given in terms of hypergeometric functions [8, 29], from which the logarithmic derivative can be directly calculated. If $r_1 > r_p$ the logarithmic derivative needs to be calculated numerically by solving equation (3) with the Dirichlet boundary condition for the upper sideband ($\xi_{r1}^{(m+1)}(\delta) = \delta^m =$ constant, with $\delta \ll 1$) and Neumann boundary condition for the lower sideband ($\frac{d}{dr}\xi_{r1}^{(m-1)}\big|_{r_-} = 0$).

This procedure leaves a degree of freedom in the solution, which is removed when taking the logarithmic derivative.

3.3.2. Main mode.

We consider the main mode perturbation localised in the low shear region, which requires $\xi_{r0}^{(m)}(r_1) \approx 0$. This follows from multiplying equation (3) with $m' = m$ by $\xi_{r0}^{(m)}$ and integrating from 0 to r_1 [2, 7, 8, 14]. This boundary condition at r_1 forces the main mode to be localised to the low shear region. This is a valid approximation since shear is known to further localise the mode, and as will be seen later in the results section, even when $q(r_1)$ is well below the rational surface the main mode remains localised in the pedestal region.

3.3.3. Vacuum boundary conditions.

The plasma is separated from an ideal metal wall by a vacuum region. The logarithmic derivative at the plasma-vacuum interface is given by [8, 27, 33] (see also appendix A)

$$\frac{r}{\xi_r^{(m')}} \frac{d\xi_r^{(m')}}{dr}\bigg|_a = \frac{2m}{m - nq_a} - \frac{m + 1 + (m-1)(a/b)^{2m}}{1 - (a/b)^{2m}},$$
(15)

where a is the minor radius of the plasma and b the radius of the ideal wall (see figure 1). This equation can be cast as a Robin boundary condition for the sidebands $m' = m \pm 1$. While this equation applies as well to the main mode perturbation $m' = m$, we will usually have $q_a \sim m/n$, which can make the logarithmic derivative arbitrarily large. To avoid this, we set $\xi_{r0}^{(m)}(a) = 0$. This can be derived by extending the definition of the plasma perturbation in the vacuum region and noticing that it can be written in a similar form as equation (3) [7, 8]. One can then follow the same procedure as at the boundary between the high shear and low shear regions, namely multiplying by ξ_{r0}^m and integrating from a to b.

4. Numerical solutions

In this section equations (14) are solved numerically. The differential operators are written in weak form, then discretised using a linear finite element scheme. The resulting matrix equations correspond to a generalised eigenvalue problem, which is solved using the Implicitly Restarted Arnoldi method built in the ARPACK [34] software package.

To empirically determine the relevance of the corrections in the safety factor, we compare three models

- *Original Exfernal model*, developed in previous work [2, 7, 8].
- *Corrected Exfernal model*, presented in this work (equation (14)).
- *Reference model*.

The relation between the 3 models is as follows. The *Reference* model is derived in the large aspect ratio approximation, obtaining equations up to order $\mathcal{O}(\epsilon^4)$. Note that no assumption on the shape of the safety factor is done for the *Reference* model, and thus is valid in the whole plasma domain. The equations are quite long and complex, and are not reported in this paper (see details in [32]). This model is the more complete of all, and provides a benchmark of the safety factor expansion done for the other two models. The *Corrected Exfernal* model assumes relatively low shear close to the rational surface. It is obtained by expanding the *Reference* model equations in the small variable $\Delta q(r)/q_s$ up to order $\mathcal{O}(\epsilon^4, \Delta q(r)^1/q_s)$ (see section 3). Finally, the *Original Exfernal* model is obtained by neglecting order $\mathcal{O}(\epsilon^4, \Delta q(r)^1/q_s)$ terms in the *Corrected Exfernal* model.

The equations are solved in the interval $[r_1, r_2]$, where r_1 and r_2 can be varied in order to maximise the growth rate [14]. It is consistently found that the three models maximise the growth rate at $r_2 = a$ independently of the shear. Growth rates with respect to variations in r_1 are shown in figure 2. Two main things happen when moving r_1 towards zero: (a) the region where the effect of mode coupling is allowed increases (destabilising) and (b) the average magnetic shear in the region where such effects are allowed is also increased (stabilising). The stability of the mode upon variations of r_1 is a competition between these two effects. Note that the stabilisation effect will be weaker if the necessary FLB effects are not included in the equations.

In the limit of zero shear it is found that the Original Exfernal model (red curve) quickly gives unphysical growth rates if $r_1 < r_p$, which is expected since the equations are only valid in the region where q is constant and close to a rational surface. Moreover, as shear is increased (figure 2(b)) the Original Exfernal model diverges even at $r_1 \geqslant r_p$. The Corrected Exfernal model (blue curve) remains close to the Reference model at small variations of r_1 even at modest shear, but as r_1 shifts to the left it slowly diverges from the Reference model (purple curve). In the Reference model the growth rate increases with r_1 moving towards zero, then saturates at around a normalised radius of $r/a \sim 0.4$–0.6. Remembering that in the interval $[0, r_1]$ the modes are taken to be independent and obey equation (3), saturation means that coupling and order $\mathcal{O}(\epsilon^4)$ effects can effectively be neglected in that interval.

Note that the Reference model is valid in the whole plasma, which means that the most accurate prediction of the growth rate must be obtained by setting $r_1 = 0$. This coincides with the maximisation of the growth rate, as coupling between the modes is mostly destabilising. Nevertheless, to be consistent when comparing the different models we set $r_1 = r_p$ and $r_2 = a$, which corresponds to the pedestal region interval.

4.1. Flat safety factor

Firstly, we study the impact of Δq corrections in the limit of zero shear by performing a parameter scan on the value of the safety factor plateau (q_*). As shown in figure 3(a) instability is found for positive and negative Δq close to the rational surface, as previously demonstrated by numerous analytical and numerical studies [2, 7, 8, 10, 11, 35]. Constant Δq corrections
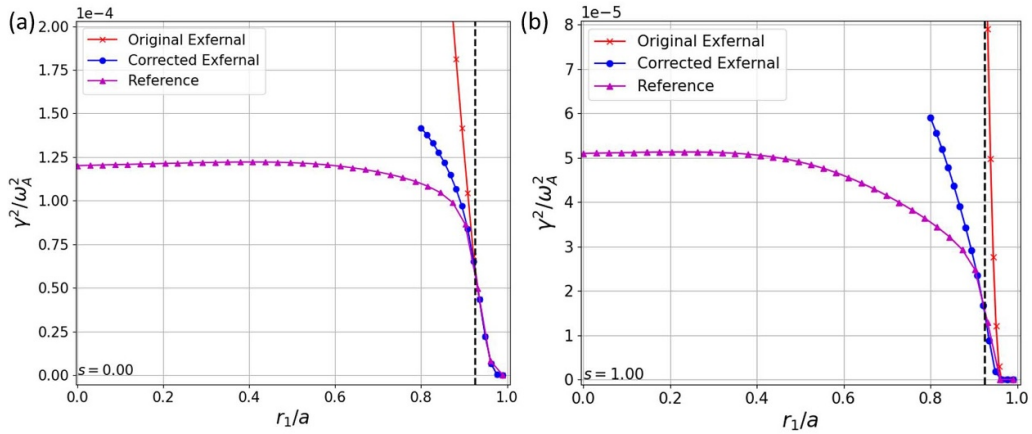
Figure 2. Growth rate as a function of the parameter r_1 at (a) $s = 0$ and (b) $s = 1$. The vertical dashed line indicates the value of r_p. The calculations adopt $\alpha = 3$, $m = 4$, $n = 1$, $q_* = 3.99$, $r_2 = a = 1$, $b = 1.3$, $a/R_0 = 1/10$, $d = 0.075$ and $r_p = a - d$. Black vertical dashed line indicates the value of r_p.
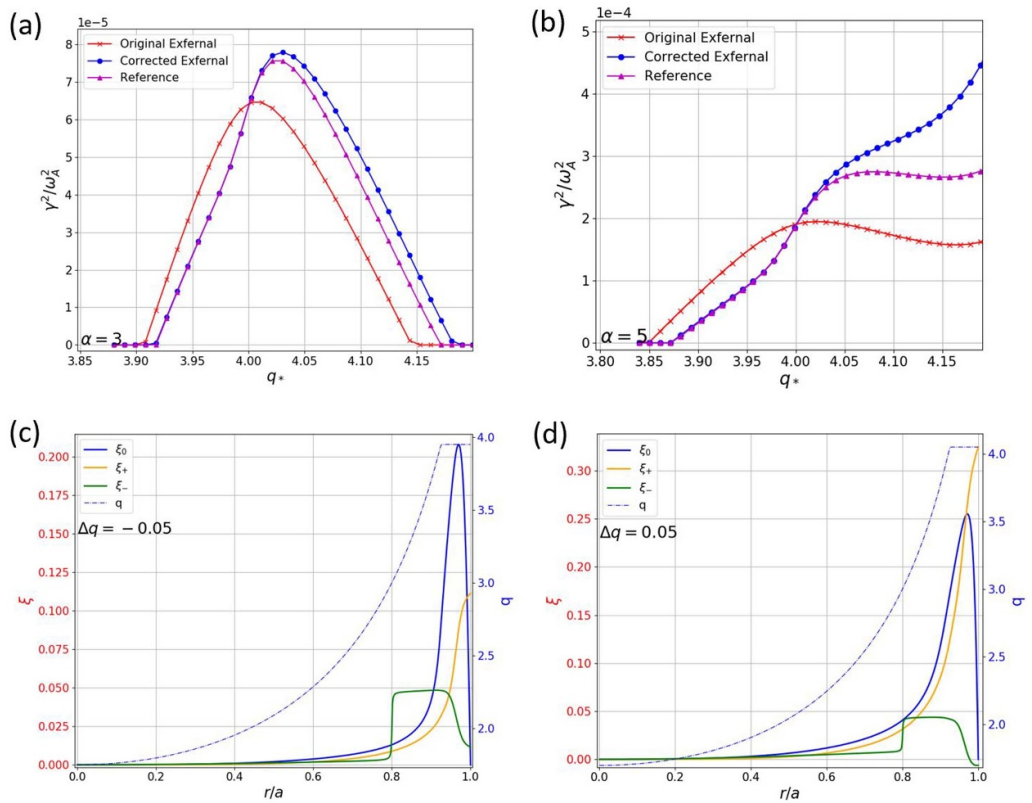

Figure 3. Growth rates as a function of q_* for (a) $\alpha = 3$ and (b) $\alpha = 5$. Radial component of the plasma displacement of the main mode (ξ_0) and sidebands ($\xi_\pm$) at (c) $\Delta q = -0.05$ and (d) $\Delta q = 0.05$. For illustration purposes we have set $r_1 = 0$ and used the *Reference* model in figures (c) and (d). Note that the main mode displacement remains localised within the pedestal region. The calculations adopt $m = 4$, $n = 1$, $b = 1.3$, $a/R_0 = 1/10$, pedestal width $d = 0.075$ and $r_p = a - d$.

have only a weak impact in the growth rate, especially where the upper sideband external kink drive is stabilising, at $q_* = q_a < q_s = q_a$. For $q_* > q_s$ the upper sideband external kink drive now provides a source of instability, enhanced through toroidal coupling with the main mode infernal drive, as reflected by the slight asymmetry in the growth rate parameter space towards positive Δq [9, 36]. This behaviour is confirmed through analysis of the plasma displacement radial profiles in

figures 3(c) and (d). For $\Delta q < 0$ the main mode is clearly dominant over the pedestal region, with the upper sideband existing only through coupling with the main mode. The opposite is true for $\Delta q > 0$, where the upper sideband is dominant. In the latter case, the main mode becomes broader and expands into the high shear region through its interaction with the upper sideband. For high enough Δq the FLB contribution of the main mode eliminates the instability completely.
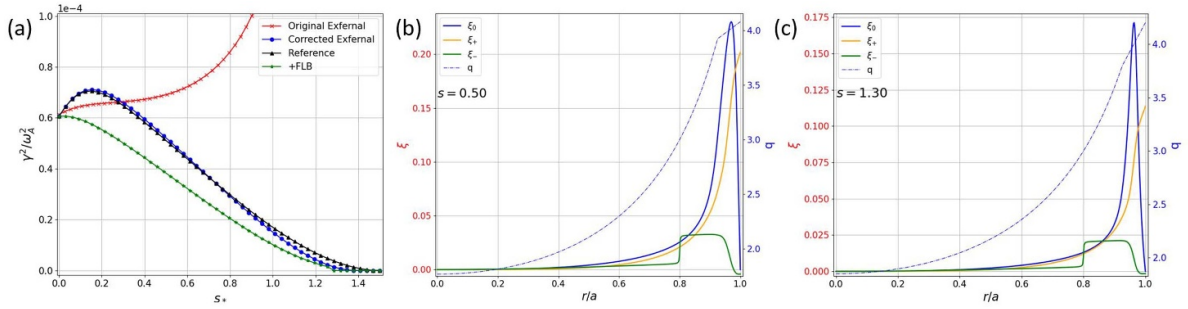
Figure 4. (a) Growth rates as a function of magnetic shear, where the line labelled as '+FLB' corresponds to the Original Exfernal model + Field Line Bending corrections to the safety factor expansion. Radial component of the plasma displacement of the main mode (ξ_0) and sidebands ($\xi_{\pm}$) at (b) $s = 0.5$ and (c) $s = 1.3$. For illustration purposes we have set $r_1 = 0$ and used the *Reference* model in figures (b) and (c). The calculations adopt $\alpha = 3$, $q_* = 4$, $m = 4$, $n = 1$, $b = 1.3$, $a/R_0 = 1/10$, pedestal width $d = 0.075$ and $r_p = a - d$.

We now increase the infernal drive by increasing the pressure gradient in the pedestal (figure 3(b)). The coupling is now strong enough to maintain the instability even for reasonably high values of Δq. When finally Δq is sufficiently high to stabilise the infernal drive, the external kink drive dominates and maintains the instability through coupling with the main mode. It should be pointed out that even when $\Delta q > 0$ the instability exists due to the coupling with the infernal drive, noting that an independent $(m + 1)/n$ external kink mode would be stable for the parameters used in these calculations. We finalise this discussion by reaffirming that Δq corrections have a weak effect in the exfernal modes at very low shear, which indicates that the Original Exfernal model provides a precise description of the instability.

4.2. Edge magnetic shear

We continue our analysis by performing a parameter scan in the magnetic shear. For this scan, stability is determined by a competition between the stabilising effect of shear and the destabilising effects of infernal and kink drives, where the kink drive is strongly influenced by the value of q_a. The computed growth rates are reported in figure 4(a). The Original Exfernal mode fails to correctly assess the effect of edge shear due to the lack of FLB stabilisation physics in the sideband equations. Moreover, the value of q_a (and so the external kink instability drive) increases with shear, which results in the mode not being stabilised by the FLB contribution of the main mode. A comparison with the results obtained using a flat safety factor confirms that the FLB stabilisation of the main mode is stronger when displacing a low-shear q-profile from the rational surface than when increasing magnetic shear.

Figure 4(a) shows that the Corrected Exfernal model gives an excellent match to the Reference model, and correctly describes the role of magnetic shear on exfernal modes. We expect the FLB contribution of the sideband to have an important role on the stabilisation of the external kink drive. To investigate further, we neglect all Δq corrections in the equations that are not related with the effect of FLB stabilisation in the sidebands. This can be somewhat justified by noting that all but one of the safety factor corrections in the main

mode equation (10) are proportional to Δq and not shear ($s \sim r\Delta q'/q_s$). For $q_* \sim q_s$ our model of the safety factor maintains a constant average $\Delta q \sim 0$ over the pedestal region upon variations of the magnetic shear, suggesting that terms proportional to Δq in the main mode equation (10) can be neglected. The resulting growth rates reproduce the main characteristic of the Reference model (green line in figure 4(a), labelled as '+FLB'), showing that FLB corrections in the sidebands are indeed what stabilises the external kink drive, and therefore the exfernal mode.

Even though the average Δq is constant over the pedestal region upon variations in the shear, the Corrected Exfernal model includes the effect of the local variation of Δq in the coupling terms. The resulting imbalance is destabilising, shifting the peak of the growth rates to $s \sim 0.2$. The effect is quickly shadowed by magnetic shear in the FLB contributions, which stabilises the mode at a limiting value of $s \sim 1.4$. The role of shear in exfernal modes is quite intuitive by analysing the radial profiles of the plasma displacement in figures 4(b) and (c). For relatively low shear ($s = 0.5$) the obtained eigenfunctions are quite similar to the case without shear, the weakening of the infernal drive being compensated by the increase of the external kink drive. Further increasing the shear reduces the infernal drive by localising the main mode around the rational surface, which in turn weakens the coupling with the sidebands and stabilises the mode.

Now that we have investigated the validity of the models and determined the important parameters in the equations, we proceed to calculate stability diagrams with physical relevance. We use the Reference model with $r_1 = 0$ and $r_2 = a$, which is the most realistic scenario. We start by producing an 'exfernal' $s - \alpha$ diagram, with s and α evaluated in the middle of the pedestal region, where α peaks. We stress that a direct comparison with the ballooning $s - \alpha$ diagram cannot be performed. In this work a particular emphasis is given to computing low-n growth rates, while the ballooning instability assumes high-n. Moreover, the shear and pressure gradient for exfernal modes are evaluated over the pedestal region, while infinite-n ballooning is dependent on the local shear and α at each flux surface. The resulting diagram using a pedestal width of $d = 0.06$ is shown in figure 5(a). It is found that
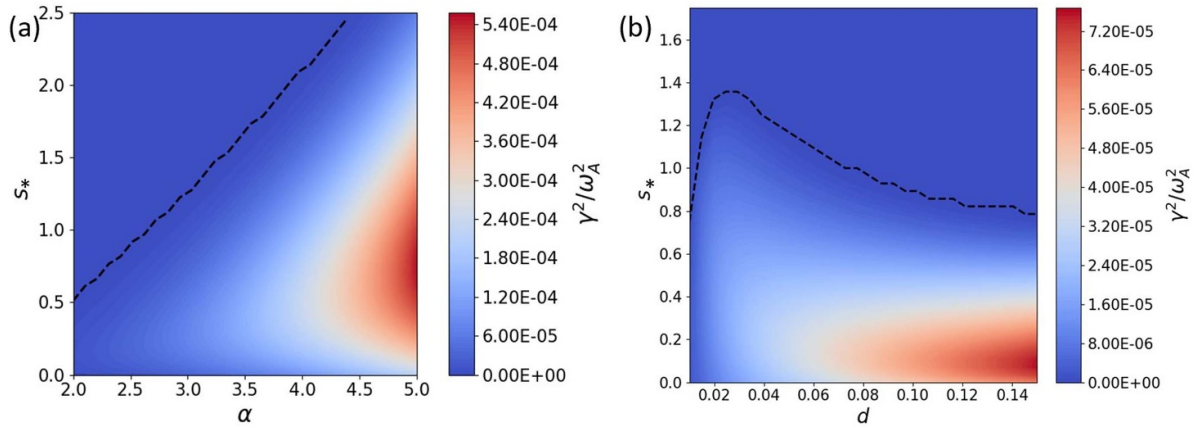
Figure 5. (a) $s - \alpha$ exfernal stability diagram with $d = 0.05$ and (b) $s - d$ exfernal stability diagram with $\alpha = 3$ at pedestal width $d = 0.06$. The dashed black line indicates in both cases the stability boundary, obtained when the numerical solution of the stability equations result in $\gamma^2 = 0$. The calculations adopt $m = 4$, $n = 1$, $b = 1.3$, $a/R_0 = 1/10$ and $r_\mathrm{p} = a - d$.

exfernal modes can support substantial shear without being stabilised, and that it increases linearly with pedestal pressure. We observe the same behaviour as in figure 4, where the growth rate peaks at non-zero shear. The peak shifts to larger values of shear with increasing α due to the stronger coupling between the modes.

QH-modes have been experimentally observed with H-mode-like pressure pedestals [23], and most recently in the wide pedestal domain [37]. We now investigate the critical shear that can be achieved for a certain pedestal width. Reducing the size of the pedestal increases the localisation of the mode, which weakens the coupling and therefore has a stabilising effect. On the other hand reducing the pedestal width increases the pressure gradient, which has a destabilising effect. To vary the pedestal width in our model we perform a scan in the parameter d, setting $r_\mathrm{p} = a - d$. We set the pressure gradient such that $\alpha = 3$ at a pedestal width of $d = 0.06$. The stability diagram is shown in figure 5(b). It is found that for a very narrow pedestal width the modes are less unstable and the critical shear is larger. Exfernal modes are more unstable for wide pedestals, but more easily stabilised by magnetic shear. This has an important implication because the current drive that weakens the shear in the pedestal region has its origin in the bootstrap current, which is proportional to the pressure gradient. A wide pedestal is associated with a lower bootstrap current, which results in higher magnetic shear over the region. On the contrary, a narrow pedestal is associated with a higher bootstrap current, which results in lower magnetic shear over the region.

5. Comparison with linear and nonlinear codes

We now compare the results of our simplified analytical model with the ones obtained by well established linear (KINX) and nonlinear (VMEC) equilibrium codes. Within the scope of this work it has been assumed that the EHOs observed during QH-mode operation correspond to the nonlinearly saturated state of exfernal modes [2, 10]. In the frame of ideal MHD and in
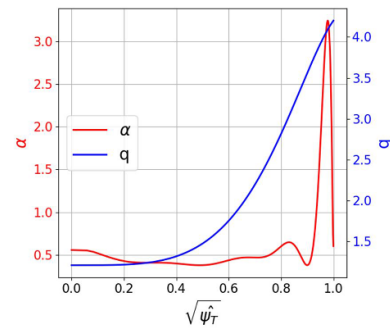

Figure 6. α and safety factor profiles used in VMEC simulations as a function of the squared root of the normalised torodial flux.

the absence of strong equilibrium flows, such states can be obtained directly from the force balance equation $\vec{J} \times \vec{B} = \nabla P$, which can be solved by the VMEC free-boundary 3D equilibrium code [38]. Boundary conditions come from the interaction of the vacuum field with the plasma, where the vacuum field is calculated through the Biot-Savart law from a set of JET-like filament coils carrying current. We look for 3D corrugated equilibrium states which have been associated with EHOs in VMEC simulations [10]. Such states are found to occur for the radial profiles shown in figure 6, in particular for a safety factor with fairly low shear on the edge region where there is a pressure pedestal. The pedestal width is roughly $d \approx 0.05$.

To isolate the effect of the infernal pressure-driven branch of the main mode, VMEC computations remove the current-driven branch of the main mode by setting $q_a > q_\mathrm{s}$ [10]. For $q_* < q_\mathrm{s}$ this is usually achieved by adding a spike to the safety factor at the edge, taking the value of q_a just above the rational surface of the main mode [9, 10]. It is argued that the spike also provides a more realistic transition between the low-shear and vacuum regions in diverted plasmas, which exhibit a sharp increase when approaching the separatrix [10]. The effect of such a spike on stability (including the spike going to infinity) will be discussed in section 6.
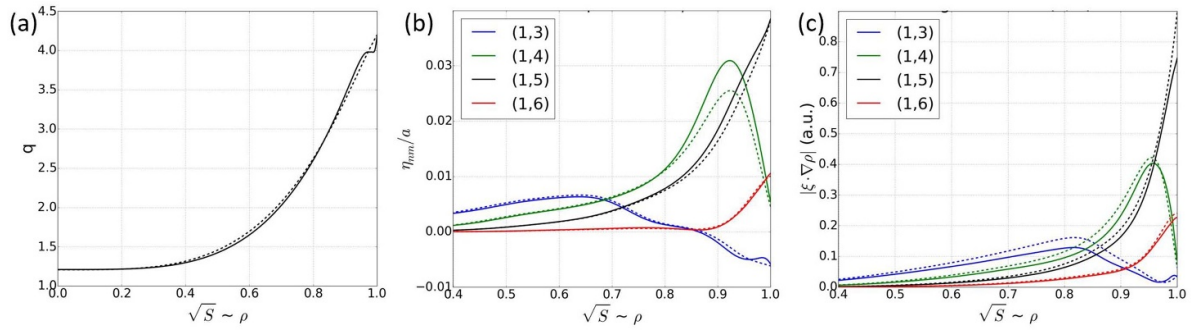
Figure 7. (a) Flat edge safety factor (solid line) and sheared safety factor (dashed line). (b) Fourier decomposition of the normalised nonlinear radial displacement calculated in VMEC. (c) Linear radial eigenfunctions calculated in KINX.

Following the methodology described in [10], we define the nonlinearly saturated radial displacement η as the normal distance between the flux surfaces of the 3D corrugated state and an equivalent neighbouring axisymmetric state, where the latter is obtained by removing all toroidal modes except $n = 0$ in the VMEC Fourier expansion. The function $\eta(r, \theta, \phi)$ is mapped to a straight coordinate system and Fourier decomposed in toroidal and poloidal modes, giving a radial profile of the nonlinear perturbed amplitude contribution of each Fourier mode.

We perform two almost identical VMEC simulations, one with a flat safety factor at the edge (solid line in figure 7(a), yielding $\gamma^2/\omega_A^2 = 0.0039$), and one with positive magnetic shear (dashed line in figure 7(a), yielding $\gamma^2/\omega_A^2 = 0.0024$). The resulting Fourier decomposition of the radial nonlinear displacement is plotted in figure 7(b) for both cases, where the solid and dashed lines correspond to the equilibria with flat edge and sheared edge safety factor respectively. Axisymmetric equivalent VMEC equilibria were then used as the basis of linear MHD stability calculations using the KINX code [39], and the linear eigenfunctions for both cases are plotted in figure 7(c). For consistency in the comparison between VMEC, KINX and our model, KINX simulations were performed without the presence of the plasma separatrix. The linear growth rates and saturated amplitudes are quite similar for the two choices of q-profiles. Linear and nonlinear simulations show that the same mode is excited, confirming the notion that exfernal modes can be excited even in the presence of modest edge magnetic shear. Notice also that the linear eigenfunctions and radial profiles of the nonlinear plasma displacement exhibit the same characteristics as the ones found by our simplified large aspect ratio model.

Finally, a series of simulations were performed for a broad scan of edge safety factor shapes. The average shear over the pedestal region was calculated and plotted in figure 8 against the KINX linear growth rate and VMEC nonlinear saturated amplitude of the $(m + 1)/n$ mode at the edge . Even though the plasma profiles and geometry is more realistic in the VMEC and KINX simulations, it is encouraging to find roughly the same limiting shear $s \sim 1.2$ as in our simplified analytical model for similar $\alpha \sim 3$ and $d \sim 0.05$.
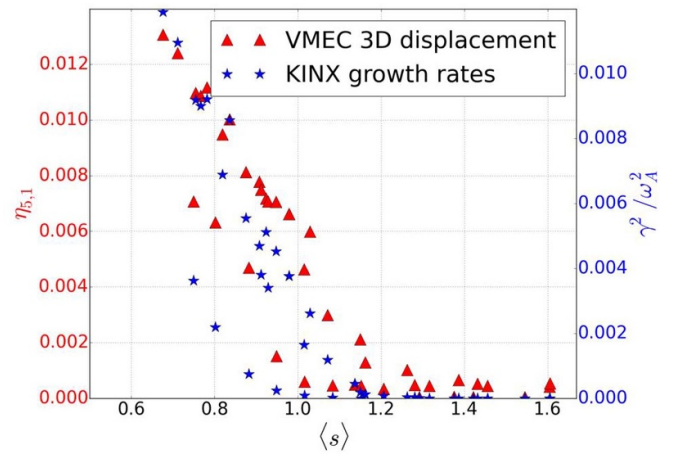

Figure 8. Amplitude of the $m + 1/n$ saturated mode calculated with VMEC (left axis) and linear growth rates (right axis) calculated with KINX. It is consistently found that the limiting shear is around unity.

6. Effect of separatrix in exfernal modes

QH-mode plasmas operate in diverted configuration, where the formation of an x-point in the edge makes the poloidal field vanish locally, resulting in $q \to \infty$ at the plasma separatrix. This has an important implication on the upper sideband external kink drive, whose rational surface now lies inside the plasma [19, 20, 22].

It is clear that the exfernal mode excitation mechanism is mostly determined by the coupling of infernal and external kink drives, with the external kink drive strongly depending on the value of q_a. The effect of q_a on edge modes has been previously studied in [40], where it was found that if q_a lies just above or just below a rational surface ($|q_a - m'/n| << 1$) the plasma becomes highly unstable and dominated by a peeling mode. Otherwise, the plasma is more stable and dominated by kink or infernal type modes. Our simplified analytical model considers three coupled poloidal harmonics. The peeling-like instability associated with the main mode (m, n) is removed by setting $\xi_{r0}^{(m)}(r_2) = 0$ at the boundary of the low shear region in order avoid an unphysically large perturbation to develop, as discussed in section 3.3. We note that we may still reach the
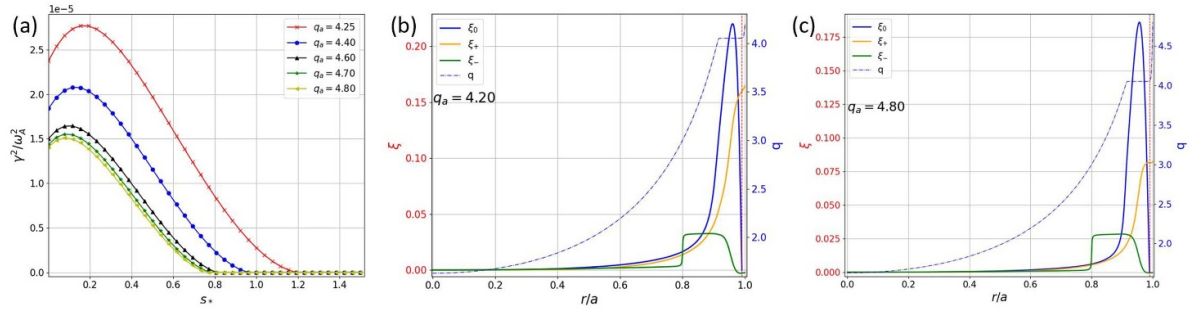
Figure 9. (a) Growth rate as a function of magnetic shear and q_a and radial component of the plasma displacement of the main mode (ξ_0) and sidebands ($\xi_{\pm}$) with (b) $q_a = 4.2$ and (c) $q_a = 4.8$. The calculations adopt $\alpha = 3$, $m = 4$, $n = 1$, $q_* = 4$, $b = 1.3$, $a/R_0 = 1/10$, $d = 0.075$, $r2 = 0.99$ and $r_p = a - d$. The separatrix region is indicated in figures (a) and (b) by the vertical red dashed line.

peeling-like instability of the $(m + 1, n)$ mode, although the growth rate should saturate before q_a is too close to $(m + 1)/n$ [40].

As a first approach to model the separatrix, the safety factor in the edge region is taken to be $q(r) = \frac{1 - s_*(r/r_*)}{A[1 - (r/a)^{\lambda}] + B}$, where $A = \frac{1 - q_* B}{q_*[1 - (r_*/a)^{\lambda}]}$, $B = \frac{1 - s_*(1 - a/r_*)}{q_a}$ and $\lambda \gg 1$. For comparison with our subsequent section, we use the Reference model with $r_1 = r_p$ and $r_2 = 0.99$, where r_2 is close to the location of sharp increase of the magnetic shear for $1 \ll \lambda = 500$. Poloidal coupling is avoided in the separatrix region due to the presence of large shear and low pressure gradient, so it is assumed that the modes obey equation (3). The boundary conditions at the plasma-vacuum interface are given by equation (15).

Figure 9(a) shows the effect of q_a as a function of magnetic shear in the pedestal region. The external kink drive of the upper sideband gets reduced due to the increased magnetic shear over the separatrix region, and growth rates saturate at $q_a \sim 4.70$. The effect of q_a on the radial components of the plasma displacement can be appreciated in figures 9(b) and (c), where an increased value of q_a reduces the external kink drive of the upper sideband. Note that since $q_a < (m + 1)/n$ the external current-driven mode has not been completely removed.

A logarithmic divergence of the safety factor is considered empirically realistic in tokamaks [41]. Therefore, to study the limit of $q_a \to \infty$ the separatrix is modelled as:

$$q(r) = \begin{cases} \dfrac{m - 1}{\kappa[1 - (r/r_-)^{\mu}] + n} & \text{if } r \leqslant r_p, \\ q_*[1 - s_*(1 - r/r_*)] & \text{if } r_p \leqslant r \leqslant r_x, \\ A \ln(a - r) & \text{if } r_x \leqslant r \leqslant a, \end{cases} \qquad (16)$$

where r_x is the radius at which the safety factor starts diverging, $r_* = (r_p + r_x)/2$ and $A = \frac{q_*[1 - s_*(1 - r_x/r_*)]}{\ln(a - r_x)}$ guarantees continuity at r_x. The dispersion relation is obtained by solving the equations in the low-shear region, where the effect of the separatrix only enters in the form of boundary conditions at the interface with the separatrix region. The upper sideband rational surface is now contained within the interval $[r_x, a]$. It

can be shown that the solution for large shear corresponds to a sum of exponential integrals of logarithmic functions, but in the limit of very small inertia within the rational layer the solution reduces to a step function. Then, the boundary condition for the upper sideband in the low shear region can be simply cast as a Neumann condition: $d\xi_{r1}^{(m+1)}/dr\big|_{r_2} = 0$. For the lower sideband, the boundary condition at r_x is obtained by solving equation (3) with $m' = m - 1$ subject to the condition in equation (15) in the limit of $q \to \infty$.

We now investigate the effect of the safety factor corrections in the presence of a plasma separatrix by comparing the three different models analysed in section 4. For consistency in the comparison, we set $r_1 = r_p$ and $r_2 = r_x$. Figure 10(a) shows the effect of the separatrix in the cases with flat safety factor (compare with figure 3(a) with no separatrix). It is clear that the separatrix reduces the parameter space for excitation of the mode as well as the value of the growth rates. Now that the external kink drive has been drastically reduced, and the instability drive comes almost exclusively from the infernal contribution. Since the external kink drive on the Original Exfernal model is now constant for any value of Δq (as the equations are now independent of q_a) the growth rates are symmetric with respect to q_s independently of the pressure gradient. The Corrected Exfernal and Reference models continue to have a slight asymmetry towards positive Δq as a result of the higher order toroidal coupling contributions. Stronger coupling induced by an increase of the pressure gradient enhances the instability and expands the excitation parameter space (figure 10(b)). Finally, an analysis of the eigenfunctions in figures 10(c) and (d) shows that the main mode is clearly dominant independently of the sign of Δq, though for $\Delta q > 0$ the upper sideband is larger than for $\Delta q < 0$.

A case of the excitation of exfernal modes in the presence of a separatrix has been previously reported in [10], where the KINX code was used to calculate the stability of QH-mode discharges in single-null diverted configuration. Even though our model of the separatrix is simplified, it reproduces all the reported characteristics in [10], namely: (a) the mode remains unstable, (b) the main mode is more localised in the pedestal
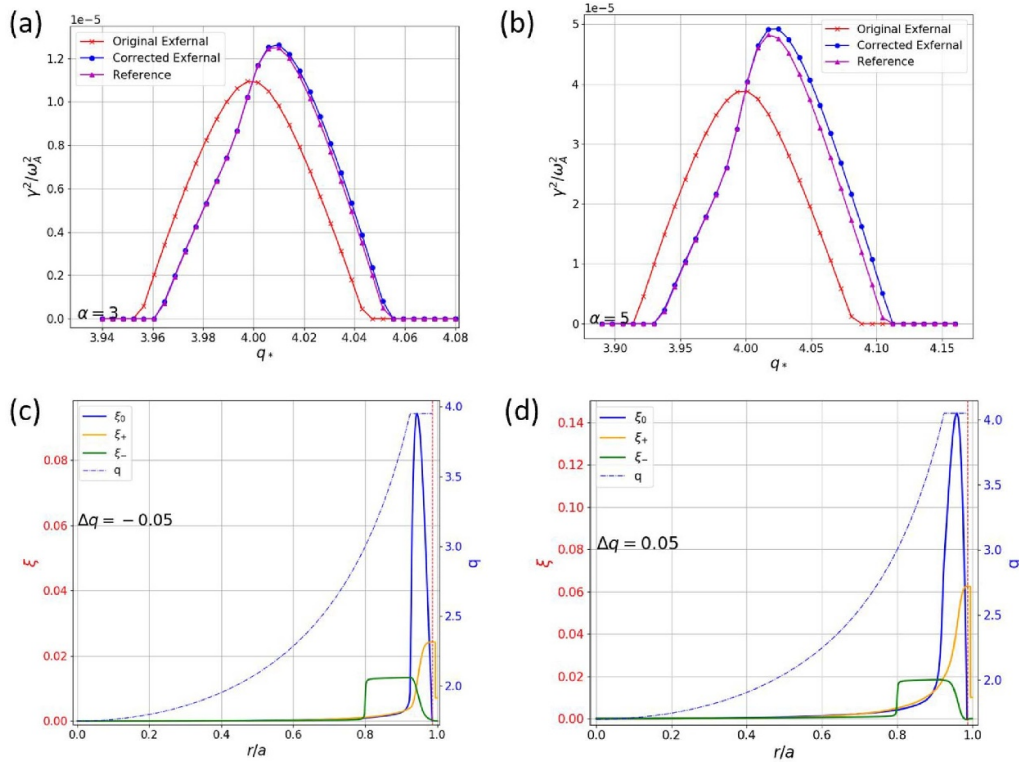
Figure 10. Growth rates as a function of q_* for (a) $\alpha = 3$ and (b) $\alpha = 5$ including a plasma separatrix. Radial component of the plasma displacement of the main mode (ξ_0) and sidebands ($\xi_\pm$) at (c) $\Delta q = -0.05$ and (d) $\Delta q = 0.05$ calculated with the Reference model and $r_1 = 0$. The vertical dashed line indicates the location of the separatrix at r_x, which has been removed only graphically for illustration purposes. The results take $m/n = 4$, $b = 1.3$, $a/R_0 = 1/10$, $d = 0.075$, $r_x = r_2 = 0.99$ and $r_p = a - d$.
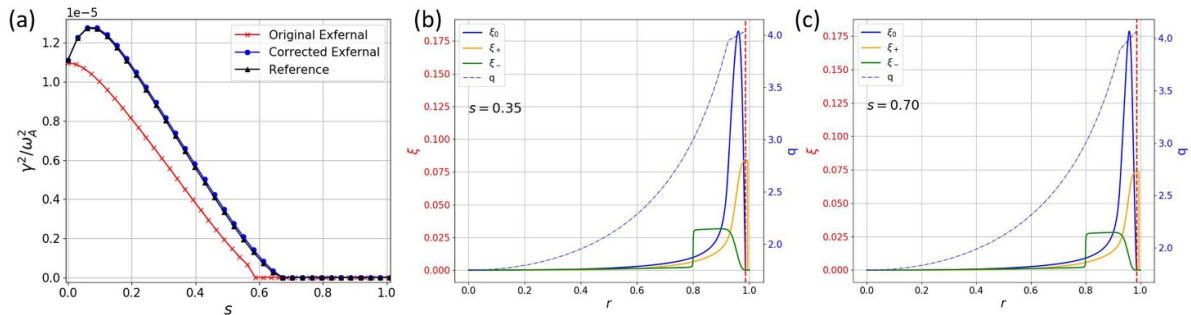

Figure 11. (a) Growth rates as a function of magnetic shear including a plasma separatrix. Radial component of the plasma displacement of the main mode (ξ_0) and sidebands ($\xi_\pm$) at (b) $s = 0.35$ and (c) $s = 0.7$ calculated with the Reference model and $r_1 = 0$. The vertical dashed line indicates the location of the separatrix at r_x, which has been removed only graphically for illustration purposes. The results take $\alpha = 3$, $q_* = 4$, $m/n = 4$, $b = 1.3$, $a/R_0 = 1/10$, $d = 0.075$, $r_x = r2 = 0.99$ and $r_p = a - d$.

than for the cases without separatrix, (c) the upper sideband has a sharp decay in the separatrix region (modelled by our step function solution), and (d) the upper sideband is slightly larger for $\Delta q > 0$.

Figure 11(a) shows that the overall effect of magnetic shear is stabilising. It is obtained once again that without the enhancement factor of the external kink drive the parameter space for exciting exfernal modes is reduced, with a critical marginal stability shear of $s \sim 0.75$. Since the destabilising sideband contributions are significantly reduced by the separatrix, the FLB contribution of the main mode in the

Original Exfernal model is enough to stabilise the mode. We can see that the Corrected Exfernal model has an excellent agreement with the Reference. The role of shear is not affected by the presence of the separatrix, as reflected by the obtained eigenfunctions (figures 11(b) and (c)): magnetic shear localises the main mode around the rational surface, weakening the infernal drive and the coupling with the sidebands.

One can note that the critical shear obtained with the 'spike' model of the safety factor saturates at $q_a < (m+1)/n$, and coincides with the critical shear obtained with the logarithmic divergence. This suggests that the sharp increase of magnetic
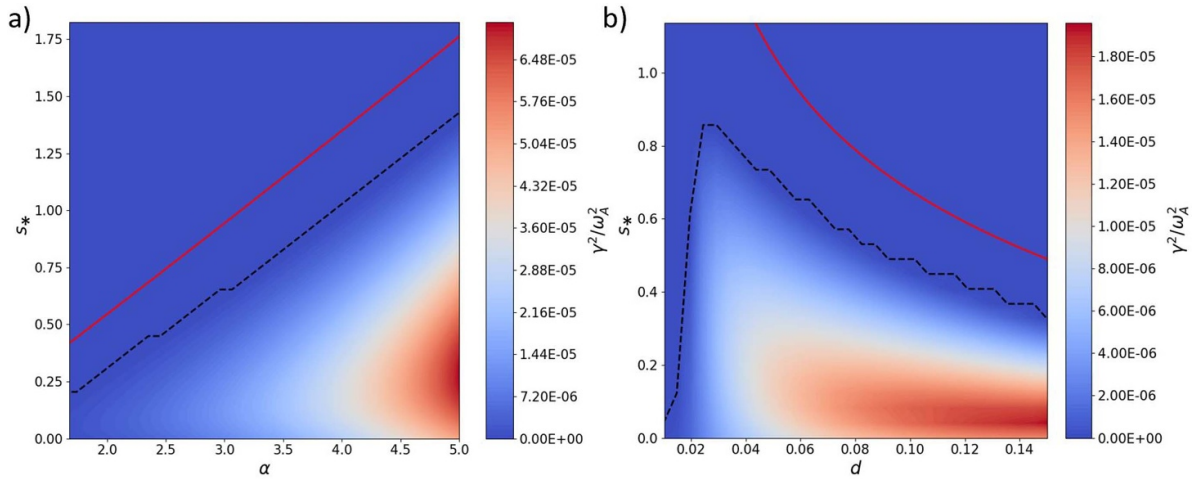
Figure 12. (a) $s - \alpha$ exfernal stability diagram with $d = 0.05$ and (b) $s - d$ exfernal stability diagram with $\alpha = 3$ at pedestal width $d = 0.06$. A model of the plasma separatrix is now included. The dashed black line indicates in both cases the stability boundary. The solid red line corresponds to the analytical estimation of the critical shear (equation (20)) calculated in section 6.1 for a linear pressure dependence in the pedestal. The results take $m/n = 4$, $b = 1.3$, $a/R_0 = 1/10$, $r_x = r_2 = 0.99$ and $r_p = a - d$.

shear is enough to significantly reduce the instability drive of the current driven branch, as suggested by previous studies [19, 22]. One can conclude that a spike in the safety factor does provide a good model for the transition between the plasma and the vacuum region in ideal MHD calculations of exfernal modes, so that more sophisticated separatrix modelling may not be needed.

We analyse the exfernal $s - \alpha$ and pedestal width stability diagrams, now introducing a separatrix using our simplified model (figures 12 (a) and (b)). The calculations use the Reference model, setting $r_1 = 0$ and $r_2 = r_x$. Since the separatrix has not affected the infernal drive of the mode, the stability diagrams show a similar behaviour as figure 5, but with the limiting shear and growth rates reduced due to the absence of the upper sideband external kink drive enhancement. Additional to the stability limit obtained numerically (dashed black line), the red solid line in figures 12(a) and (b) show an analytical estimation of the marginal magnetic shear. The derivation is obtained with a simple model presented in the next subsection.

6.1. Analytical estimation of edge critical shear

For simplicity we consider the Original Exfernal model, which has been shown to describe fairly well the effect of magnetic shear, and to give a good estimate of its critical value for instability in plasmas with separatrix. Recalling that the Original Exfernal model neglects corrections of order $\mathcal{O}(\epsilon^4, \Delta q^1)$, we can readily integrate equation (11) and substitute into equation (10) to obtain [7, 8, 14]:

$$\frac{d}{dr}\left[r^3 Q^2 \frac{d}{dr}\xi_{r0}^{(m)}\right] - r(m^2 - 1)\left[Q^2 + r\frac{d}{dr}\bar{\gamma}^2\right]\xi_{r0}^{(m)}$$
$$+ \frac{r\alpha}{R_0 q_s^2}\left(\frac{1}{q_s^2} - 1\right)\xi_{r0}^{(m)} + \frac{\alpha}{2q_s^2}\sum_{\pm}\frac{r^{1\pm m}}{1\pm m}L_{\pm} = 0, \quad (17)$$

where $Q^2 = (1/q - 1/q_s)^2 + \bar{\gamma}^2$, $\bar{\gamma}^2 = \gamma^2(1 + 2q_s^2)/(\omega_A^2 m^2)$ and $L_{\pm}$ are the constants of integration that account for the coupling with the neighbouring sidebands. $L_{\pm} = \Lambda_{\pm}\int_{r_p}^{r_x}\alpha r^{1\pm m}\xi_{r0}^{(m)}dr$, where $\Lambda_{\pm}$ are defined in a similar way as in [7, 8, 14] (see appendix B). Let us define $h = d/(2r_*) \ll 1$ and assume that in the pedestal region the pressure and mass density profiles depend linearly on r so that α is constant. Thus, we approximate $\int_{r_p}^{r_x}\alpha r^{1\pm m}\xi_{r0}^{(m)}dr \approx \alpha r_*^{1\pm m}\int_{r_p}^{r_x}\xi_{r0}^{(m)}dr$. For the sake of convenience, we impose the normalisation $\int_{r_p}^{r_x}\xi_{r0}^{(m)} = 1$, which consequently formally yields $\xi_{r0}^{(m)}/a \sim h^{-1}$.

By introducing the variable $x = (r - r_*)/r_*$ and expanding around $x = 0$, the mass density and pressure are written as $\rho/\rho_p = P/P_p = (h - x)/(2h)$, where $\rho_p = \rho(r_p)$ and $P_p = P(r_p)$ are the values at the pedestal top. Taking $q(r_*) = q_s = m/n$ and expanding equation (17) around $x = 0$ reduces to

$$\frac{d}{dx}\left[f\frac{d}{dx}\xi_{r0}^{(m)}\right] + \frac{r\alpha}{R_0}\left(\frac{1}{q_s^2} - 1\right)\xi_{r0}^{(m)} + \frac{\alpha}{2}\sum_{\pm}\frac{r_*^{\pm m}}{1\pm m}L_{\pm} = 0 \quad (18)$$

where $f = s_*^2 x^2 + \gamma^2 \tau_A^2\left(\frac{h-x}{2h}\right)$ with $s_* = rq'/q|_{r_*}$ and $\tau_A^2 = \frac{1}{(\omega_A(r_p)n)^2}(1 + 2q_s^2)$. Let us define the constant $U = \frac{\alpha}{2}\sum_{\pm}\frac{r_*^{\pm m}L_{\pm}}{1\pm m}$. A rough estimate of the critical magnetic shear can be obtained by balancing the field line bending and coupling terms in the equation above, in the limit of $\gamma \to 0$ and under the assumption that the Mercier contribution is small (this will be proven later). Hence, assuming that $\frac{d}{dx} \sim \frac{1}{x} \sim \frac{1}{ah}$ and using the normalisation condition for $\xi_{r0}^{(m)}$, the critical magnetic shear scales as $s_*^2 \sim ahU$. The solution to equation (18) can be written in terms of hypergeometric functions (see [29]). Requiring that $\xi_{r0}^{(m)}$ vanishes at $x = \pm h$, imposing the normalisation condition for $\xi_{r0}^{(m)}$ in the solution and

taking the limit of $\gamma \to 0$ yields the condition for marginal stability

$$1 = \frac{2hr_*U}{\mathcal{D}} \left(1 - \frac{1}{2} \frac{\Gamma\left(\frac{1}{4} + \frac{1}{4}\sqrt{1 + \frac{4\mathcal{D}}{\hat{s}^2}}\right)}{\Gamma\left(\frac{5}{4} + \frac{1}{4}\sqrt{1 + \frac{4\mathcal{D}}{\hat{s}^2}}\right)} \right), \quad (19)$$

where $\mathcal{D} = \frac{r_*\alpha}{R_0}\left(1 - \frac{1}{q_s^2}\right)$ is the Mercier contribution and Γ is the Gamma function. We note that the Mercier contribution is proportional to $\epsilon\alpha\xi_{r0}^{(m)}$, whereas the coupling contribution scales as α^2. Assuming $\epsilon\xi_{r0}^{(m)}/a \sim \epsilon h^{-1} \sim 1$, it turns out that for sufficiently large pressure gradients the coupling contribution dominates over the weakly stabilising Mercier term, allowing us to expand equation (19) in the limit of $\mathcal{D} \ll 1$, finally giving

$$s_* = \sqrt{2hr_*U} - \frac{\mathcal{D}}{\sqrt{2hr_*U}}. \quad (20)$$

This expression has the very same dependencies on the rough scaling obtained previously, balancing field line bending and coupling contributions. Evaluating U requires expressions for the constants $\Lambda_\pm$. It can be shown (see appendix B) that $U \approx \frac{7}{12r_*}m\alpha^2$, so that $s_* \approx \alpha\sqrt{\frac{7}{6}hm} - \frac{\mathcal{D}}{\alpha\sqrt{\frac{7}{6}hm}}$. Recalling that $\mathcal{D} \propto \alpha$, this expression immediately recovers the linear dependency of the critical shear on pedestal pressure obtained numerically by the Reference model (figure 12(a)). Note that in the limit of $\alpha \to 0$, the only stabilising effect at zero shear comes from the Mercier term, meaning that without it, any pedestal pressure would excite an exfernal instability for the case of $q_* = q_s$ and zero shear. This result was verified by removing the Mercier contribution in the Corrected Exfernal model and solving the equations numerically.

Substituting the parameters used in the calculations above gives the marginal magnetic shear $s_* = 0.382\alpha - 0.233$ (solid red line in figure 12(a)), whose dependence upon the parameter α is remarkably close to the one obtained by a linear fit of the numerical results shown in figure 12(a) ($s_* = 0.368\alpha - 0.447$). Note that the numerical results in figure 12(a) were obtained with a tanh-like pressure profile (α corresponding to the peak value within the pedestal), while the analytical estimation assumes a constant α. This results in an overestimation of the critical shear by equation (20). Solving the Original Exfernal equations numerically using a linear pressure profile in the pedestal region gives a better match to our analytical estimation (see figure B1 in appendix B).

Expressing α in terms of h allows a study into the critical shear as a function of pedestal width at constant pedestal pressure. Since $\alpha \sim 1/h$ and thus $\hat{s} \sim h^{-1/2}$, our simple analytical formula recovers as well the correct dependency of critical shear on pedestal width in figure 12(b), except for small pedestal widths.

A final analytical estimation links the toroidal current density to the critical shear through the relation in cylindrical limit $J_{\text{tor}} = \frac{B_0}{rR_0}\frac{d}{dr}\left(\frac{r^2}{q}\right)$. Expanding this expression and plugging the value for the magnetic shear computed in equation (20), we

obtain the following value of the required pedestal current density for the EHO excitation

$$J_{\text{tor}} \approx \frac{2B_0}{q_*R_0}\left(1 - \sqrt{\frac{hr_*U}{2}} + \frac{P}{2\sqrt{2hr_*U}}\right). \quad (21)$$

We stress that equation (21) is valid in a cylindrical limit and variations are expected for more accurate toroidal diverted geometry.

7. Summary and conclusions

In this work the effect of finite edge shear on the excitation mechanism of exfernal modes has been investigated by deriving new differential equations describing infernal modes at the edge of a large aspect ratio tokamak plasma expansion. Such equations correspond to an extension of the original exfernal model, where we have included higher order $\Delta q/q_s$ terms in the safety factor expansion. The equations were solved numerically for equilibrium profiles containing key physical elements observed during QH-mode operation. The obtained solution was compared with the Original Exfernal model and with a Reference model, where the later was obtained by retaining the full safety factor in the leading order stability equations.

We find that the parameter space for the excitation of exfernal modes depends mainly on the interplay between the edge infernal drive of the main mode and the external kink drive of the upper side band. The Original Exfernal model includes all the relevant physics to properly resolve the instability for the case of very low shear, but fails to predict the effect of edge magnetic shear due to the absence of FLB cylindrical corrections in the sideband equations. Adding such corrections gives a good qualitative picture of the shear dependency of the instability, while higher order $\Delta q/q_s$ toroidal corrections have a destabilising effect on the mode.

A comparison between our model and linear (KINX) and nonlinear (VMEC) codes was performed. It was found that exfernal modes can be unstable in the presence of finite edge shear, and the critical shear for exciting such modes agrees well with the one found by our simplified large aspect ratio model. We can conclude that while exfernal modes are stabilised by magnetic shear, its effect is somewhat weak, allowing the excitation of the mode at modest edge magnetic shear in QH-mode-like pedestals. This relaxes the previous assumption of having a flat safety factor in the near vicinity of a rational surface at the edge.

The vacuum boundary conditions were later modified to include a plasma separatrix. Our simplified model finds that the presence of an x-point is stabilising by significantly reducing the external kink drive of the upper sideband. In this case the $\Delta q/q_s$ corrections in the sideband equations can be neglected, and the Original Exfernal model gives a good estimation of the growth rates and critical shear. Nevertheless, the excitation of the mode is robust and sustained by the infernal drive, though the growth rates and the instability parameter space are reduced. Even then, we find that the mode can

support a magnetic shear of order unity at modest values of pressure gradient ($\alpha \sim 4$) and a typical pedestal width of $d \sim 0.06$. It is important to point out that a more accurate model of the separatrix might change this behaviour. For example, the infernal drive can be enhanced by the presence of kink-tearing modes, which have been found to be unstable in the presence of a separatrix [20]. Also, in cases with and without separatrix, the Corrected Exfernal model presented in this work produces an excellent match with the reference case, meaning that the equations presented in this paper should be enough to describe the stability of exfernal modes in the large aspect ratio approximation.

Our calculations neglect $\vec{E} \times \vec{B}$ flow, arguing that it weakly affects low-n modes [17], assuming also that its effect is independent of that of edge magnetic shear. In a more refined study the latter assumption might be relaxed. For example, as shown in [3], $\vec{E} \times \vec{B}$ stabilisation of high-n modes is stronger for large edge current density (or equivalently low edge magnetic shear), which might impose a more severe constraint on the critical shear for marginal stability than the one calculated in this paper.

EHOs are found to have a broad radial structure [17] covering the whole pedestal. Even though the presence of magnetic shear localises the main mode around the rational surface, we have found that at moderate edge shear ($s \sim 0.5 - 1.$) the broad radial structure is sustained by coupling with the upper side-band kink drive. When the localisation of the mode is strong such as in high edge shear cases ($s \gtrsim 1.5$) or in the presence of a plasma separatrix, another mechanism is required to maintain the broadening of the main mode. In this respect, it has been found that $\vec{E} \times \vec{B}$ flow shear can cause radial expansion of the mode structure [18].

The model presented in this work helps to better understand the restrictions on the excitation mechanism of edge infernal modes, and has possible applications for the development of QH-mode scenarios in current and future tokamaks. Other effects that could induce or facilitate the excitation of exfernal modes, such as plasma shaping and interaction with external magnetic perturbations will be presented in future publications.

Data availability statement

All data that support the findings of this study are included within the article (and any supplementary files).

Acknowledgment

Appendix A. Vacuum boundary conditions

The plasma is separated from a perfectly conducting wall by a vacuum region. Jump conditions at the plasma-vacuum interface read [27, 42]:

$$\llbracket \delta p + \vec{B} \cdot \delta \vec{B} \rrbracket_a = 0 \tag{A.1}$$

$$\llbracket \hat{n} \cdot \delta \vec{B} \rrbracket_a = 0. \tag{A.2}$$

The perturbed vacuum magnetic field must fulfil the condition $\nabla \times \delta \vec{B}_V = 0$, which allows us to write $\delta \vec{B}_V = \nabla \Phi$. Since $\nabla \cdot \delta \vec{B}_V = 0$, we have that $\nabla^2 \Phi = 0$. Assuming $\Phi(r, \theta, \phi) = \hat{\Phi}(r) e^{-i(m\theta - n\phi)}$ we have the following equation to leading order for $\hat{\Phi}(r)$

$$\frac{d}{dr}\left[r \frac{d\hat{\Phi}}{dr} \right] - m^2 \hat{\Phi} = 0, \tag{A.3}$$

with solution

$$\hat{\Phi}(r) = A \left[(r/b)^m + (r/b)^{-m} \right], \tag{A.4}$$

where we have already applied the ideal wall boundary condition $\hat{n} \cdot \delta \vec{B}_V = 0 \big|_b$. Assuming no equilibrium skin currents, the equilibrium vacuum magnetic field equals the plasma magnetic field at the interface, $\vec{B}_V(a) = \vec{B}(a)$. We then have, to leading order in the vacuum side of the interface ($r = a + \delta$):

$$\vec{B}(a) \cdot \delta \vec{B}_V(a) = -A \frac{iB_0}{R_0 q_a}(m - nq_a) \left[(a/b)^m + (a/b)^{-m} \right] \tag{A.5}$$

$$\hat{n} \cdot \delta \vec{B}_V(a) = A \frac{m}{a} \left[(a/b)^m - (a/b)^{-m} \right], \tag{A.6}$$

and in the plasma side of the interface ($r = a - \delta$):

$$\delta P(a) + \vec{B}(a) \cdot \delta \vec{B}(a) = -\frac{aB_0}{m^2 q_a R_0^3}(m - nq_a)$$

$$\left[(m - nq_a)a \frac{d\xi_r^{(m')}}{dr}(a) - (m + nq_a)\xi_r^{(m')}(a) \right] \tag{A.7}$$

$$\hat{n} \cdot \delta \vec{B}(a) = -\frac{i}{R_0^2 q_a}(m - nq_a)\xi_r^{(m')}(a). \tag{A.8}$$

Taking $\frac{\delta P(a) + \vec{B}(a) \cdot \delta \vec{B}(a)}{\hat{n} \cdot \delta \vec{B}(a)} = \frac{\vec{B}(a) \cdot \delta \vec{B}_V(a)}{\hat{n} \cdot \delta \vec{B}_V(a)}$ eliminates the constant A and ultimately gives [8, 27, 33]

$$\frac{r}{\xi_r^{(m')}} \frac{d\xi_r^{(m')}}{dr}\bigg|_a = \frac{2m}{m - nq_a} - \frac{m + 1 + (m - 1)(a/b)^{2m}}{1 - (a/b)^{2m}}. \tag{A.9}$$

Appendix B. Analytical estimation of *U*

As found in the literature [7, 8, 14], the constants $\Lambda_\pm$ are given by

$$\Lambda_{\pm} = \frac{(1 \pm m)^2 [2 \pm m + \mathcal{B}_{\pm}(r_{\mathrm{p}})][2 \pm m + \mathcal{B}_{\pm}(r_x)] r_x^{-2(1 \pm m)}}{(\pm m - \mathbf{B}_{\pm}(r_x))[2 \pm m + \mathcal{B}_{\pm}(r_{\mathrm{p}})] - \left(\frac{r_{\mathrm{p}}}{r_x}\right)^{2(1 \pm m)} (\pm m - \mathcal{B}_{\pm}(r_{\mathrm{p}}))(2 \pm m \mathcal{B}_{\pm}(r_x))}, \tag{B.1}$$
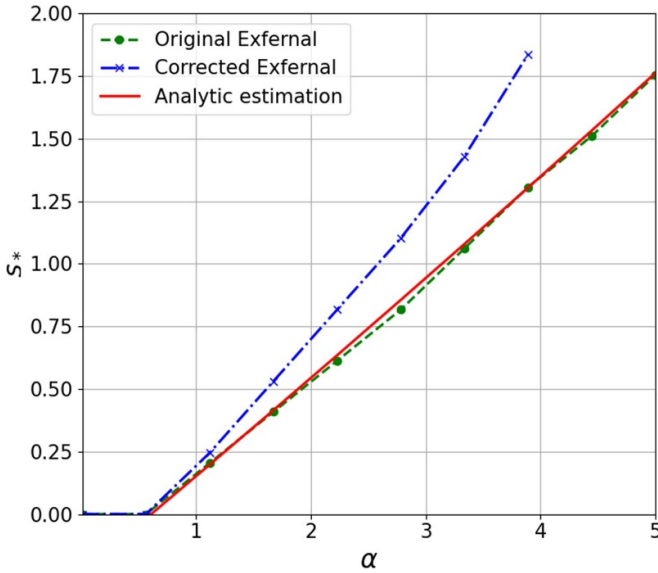

Figure B1. Comparison of the critical shear obtained the Original Exfernal model (blue line), Corrected Exfernal model (green line) and the analytical estimation (equation (20)) using a linear pressure profile in the pedestal ($P/P_0 = (h - x)/(2h)$). The calculations adopt $m = 4$, $n = 1$, $b = 1.3$, $d = 0.06$, $a/R_0 = 1/10$, $r_{\mathrm{p}} = a - d$, $r_x = 0.988$, $r_1 = r_x - d$ and $r_2 = r_x$.

where $\mathcal{B}_{\pm}(r) = r \frac{d}{dr} \ln \left[\xi_{r0}^{(m \pm 1)}(r) \right]$. From previous computations performed with a simplified step-model for the curent density and a sufficiently distant wall [2, 7], we have $\mathcal{B}_{+}(r_{\mathrm{p}}) \approx 3m + 2$, $\mathcal{B}_{-}(r_{\mathrm{p}}) \approx m/6 - 1/4$ and $\mathcal{B}_{+}(r_x) \approx 2 - 3m$. The Neumman boundary condition for the upper sideband at the interface between the pedestal and separatrix regions means $\mathcal{B}_{+}(r_x) = 0$. It is worth pointing out that a more refined computation with a diffuse current profile does not give too different results [43]. This specifies completely the coupling coefficient U through the constants $L_{\pm}$, so that

$$r_* U \approx \alpha^2 \left[\frac{(m+1)(m+2)}{2m + (2+m)Y} \left(\frac{r_*}{r_x}\right)^{2(1+m)} + \frac{(m-1)(m-2)}{m - 2 + 3mZ} \left(\frac{r_*}{r_x}\right)^{2(1-m)} \right], \tag{B.2}$$

where $Y = (r_{\mathrm{p}}/r_x)^{2(1+m)}$ and $Z = (r_{\mathrm{p}}/r_x)^{2(1-m)}$. In the limit of m not too large and narrow pedestal width, we may approximate $r_* U \approx \frac{7}{12} m \alpha^2$. Figure B1 shows the analytical estimation obtained by inserting this expression into equation (20), and is compared with the analytical estimation obtained from

the numerical solution using the Original Exfernal and Corrected Exfernal models. In this case, a linear pressure profile in the pedestal region was adopted in the numerical calculations to have a better comparison with the analytical solution. The excellent match in the critical shear between the Original Exfernal model and the analytical estimation confirms that the approximations taken in the derivation of equation (20) are valid in these simplified cases. The Corrected exfernal model prediction of the critical shear is close to the analytical estimation for low α. As pressure gradient increases the destabilising order $\mathcal{O}(\epsilon^4, \Delta q/q_{\mathrm{s}})$ coupling corrections (which are not included in the analytical estimation) become stronger, separating the analytical estimation from the one of the Corrected Exfernal model.

ORCID iDs

G Bustos Ramirez ⬤ https://orcid.org/0000-0002-8817-5344
J P Graves ⬤ https://orcid.org/0000-0002-7959-7959
D Brunetti ⬤ https://orcid.org/0000-0001-8650-3271

References

[1] Burrell K H *et al* 2001 Quiescent double barrier high-confinement mode plasmas in the DIII-D tokamak *Phys. Plasmas* **8** 2153–62

[2] Brunetti D, Graves J P, Lazzaro E, Mariani A, Nowak S, Cooper W A, and Wahlberg C 2019 Excitation mechanism of low-n edge harmonic oscillations in edge localized mode-free, high performance, tokamak plasmas *Phys. Rev. Lett.* **122** 155003

[3] Chen J G, Xu X Q, Ma C H, Xi P W, Kong D F, and Lei Y A 2017 Impact of E × B shear flow on low-n MHD instabilities *Phys. Plasmas* **24** 050704

[4] Liu F, *et al* 2018 Nonlinear MHD simulations of QH-mode DIII-D plasmas and implications for ITER high Q scenarios *Plasma Phys. Control. Fusion* **60** 014039

[5] Dong G Q, Liu Y Q, Liu Y, Wang S, Zhang N, Hao G Z, and Xia G L 2019 Non-linear interplay between edge localized infernal mode and plasma flow *Nucl. Fusion* **59** 066011

[6] Pankin A Y, King J R, Kruger S E, Chen X, Burrell K H, Garofalo A M, Groebner R J, McKee G R, and Yan Z 2020 Towards validated MHD modeling of edge harmonic oscillation in DIII-D QH-mode discharges *Nucl. Fusion* **60** 092004

[7] Brunetti D, Graves J P, Lazzaro E, Mariani A, Nowak S, Cooper W A, and Wahlberg C 2018 Analytic stability criteria for edge MHD oscillations in high performance ELM free tokamak regimes *Nucl. Fusion* **58** 014002

[8] Brunetti D, Graves J P, Lazzaro E, Mariani A, Nowak S, Cooper W A, and Wahlberg C 2018 Analytic study on low-n external ideal infernal modes in tokamaks with large edge pressure gradients *J. Plasma Phys.* **84** 1–22

[9] Zheng L J, Kotschenreuther M T, and Valanju P 2013 Low-n magnetohydrodynamic edge instabilities in quiescent H-mode plasmas with a safety-factor plateau *Nucl. Fusion* **53** 063009

[10] Kleiner A, Graves J P, Brunetti D, Cooper W A, Medvedev S, Merle A, and Wahlberg C 2019 Current and pressure gradient triggering and nonlinear saturation of low-n edge harmonic oscillations in tokamaks *Plasma Phys. Control. Fusion* **61** 084005

[11] Dong G Q, Liu Y Q, Wang S, Zhang N, Yu D L, Liu Y, and Wang Z R 2017 Stability of ideal and non-ideal edge localized infernal mode *Phys. Plasmas* **24** 112510

[12] Garofalo A M *et al* 2015 The quiescent H-mode regime for high performance edge localized mode-stable operation in future burning plasmas *Phys. Plasmas* **22** 056116

[13] Han R, Zhu P, Banerjee D, Cheng S, Yan X, and Zheng L and Cfetr Physics Team 2020 Low-n global ideal MHD instabilities in the CFETR baseline scenario *Plasma Phys. Control. Fusion* **62** 13

[14] Gimblett C G, Hastie R J, and Hender T C 1996 An analytic study of the magnetohydrodynamic stability of inverse shear profiles *Phys. Plasmas* **3** 3369–74

[15] Garofalo A M *et al* 2011 Advances towards QH-mode viability for ELM-stable operation in ITER *Nucl. Fusion* **51** 083018

[16] Liu F, Huijsmans G T, Loarte A, Garofalo A M, Solomon W M, Snyder P B, Hoelzl M, and Zeng L 2015 Nonlinear MHD simulations of quiescent H-mode plasmas in DIII-D *Nucl. Fusion* **55** 113002

[17] Chen X *et al* 2016 Rotational shear effects on edge harmonic oscillations in DIII-D quiescent H-mode discharges *Nucl. Fusion* **56** 076011

[18] Xu G S 2017 E × B flow shear drive of the linear low-n modes of EHO in the QH-mode regime *Nucl. Fusion* **57** 086047

[19] Webster A J and Gimblett C G 2009 Magnetohydrodynamic stability of a toroidal plasma's separatrix *Phys. Rev. Lett.* **102** 035003

[20] Huysmans G T 2005 External kink (peeling) modes in x-point geometry *Plasma Phys. Control. Fusion* **47** 2107–21

[21] Huysmans G T A and Czarny O 2007 MHD stability in x-point geometry: simulation of ELMs *Nucl. Fusion* **47** 659–66

[22] Saarelma S, Kwon O J, and Kirk A 2011 X-point effect on edge stability *Plasma Phys. Control. Fusion* **53** 025011

[23] Burrell K H 2005 Advances in understanding quiescent H-mode plasmas in DIII-D *Phys. Plasmas Am. Inst. Phys.* **12** 056121

[24] Greene J M and Chance M S 1981 The second region of stability against ballooning modes *Nucl. Fusion* **21** 453–64

[25] Connor J W, Hastie R J, and Taylor J B 1978 Shear, periodicity, and plasma ballooning modes *Phys. Rev. Lett.* **40** 396–99

[26] Hastie R J and Hender T C 1988 Toroidal internal kink stability in tokamaks with ultra flat q profiles *Nucl. Fusion* **28** 585

[27] Freidberg J P 2014 *Ideal MHD* vol 1 (Cambridge: Cambridge University Press)

[28] Newcomb W A 1960 Hydromagnetic stability of a diffuse linear pinch *Ann. Phys.* **10** 232–67

[29] Mikhailovskii A B 2017 *Instabilities in a Confined Plasma* (Boca Raton, FL: CRC Press)

[30] Bussac M N, Pellat R, Edery D, and Soule J L 1975 Internal kink modes in toroidal plasmas with circular cross sections *Phys. Rev. Lett.* **35** 1638–41

[31] Graves J P, Zullino D, Brunetti D, Lanthaler S, and Wahlberg C 2019 Reduced models for parallel magnetic field fluctuations and their impact on pressure gradient driven MHD instabilities in axisymmetric toroidal plasmas *Plasma Phys. Control. Fusion* **61** 104003

[32] Graves J P *et al* 2021 Pressure driven long wavelength MHD instabilities in an axisymmetric toridal resistive plasma *Sub to Plasma Physics and Controlled Fusion*

[33] Wesson J A 1978 Hydromagnetic stability of tokamaks *Nucl. Fusion* **18** 1

[34] Lehoucq R, Maschhoff K, Sorensen D, and Yang C 1997 *ARPACK: Solution of Large Scale Eigenvalue Problems with Implicitly Restarted Arnoldi Methods* (New York: Academic)

[35] Wahlberg C and Graves J P 2007 Stability analysis of internal ideal modes in low-shear tokamaks *Phys. Plasmas* **14** 110703

[36] Kleiner A, Graves J P, Cooper W A, Nicolas T, and Wahlberg C 2018 Free boundary 3D ideal MHD equilibrium calculations for non-linearly saturated current driven external kink modes in tokamaks *Nucl. Fusion* **58** 074001

[37] Diii-D Team T *et al* 2017 Stationary QH-mode plasmas with high and wide pedestal at low rotation on DIII-D *Nucl. Fusion* **57** 022007

[38] Hirshman S P and Whitson J C 1983 Steepest-descent moment method for three-dimensional magnetohydrodynamic equilibria *Phys. Fluids* **26** 3553–68

[39] Degtyarev L, Martynov A, Medvedev S, Troyon F, Villard L, and Gruber R 1997 The KINX ideal MHD stability code for axisymmetric plasmas with separatrix *Comput. Phys. Commun.* **103** 10–27

[40] Zheng L J, Kotschenreuther M T, and Valanju P 2017 The sensitivity of tokamak magnetohydrodynamics stability on the edge equilibrium *Phys. Plasmas* **24** 102503

[41] Webster A J 2009 Magnetohydrodynamic stability at a separatrix II. Determination by new conformal map technique *Phys. Plasmas* **16** 082503

[42] Glasstone Samuel L R H 1960 *Controlled Thermonuclear Reactions: An Introduction to Theory and Experiment* (Princeton, NJ: Van Nostrand)

[43] Brunetti D, Graves J P, Cooper W A, and Wahlberg C 2014 Fast growing resistive two fluid instabilities in hybrid-like tokamak configuration *Plasma Phys. Control. Fusion* **56** 075025